# Sorption model for yttrium in fluorapatite: Geochemical implications

C Bonnet, M Muñoz, O Mathon, V Motto-Ros, A Elghali, F Parat, Jérémie Aubineau, J-L Bodinier

Geochemical Perspectives Letters



# Sorption model for yttrium in fluorapatite: Geochemical implications

C. Bonnet[1,2*], M. Muñoz[1], O. Mathon[2], V. Motto-Ros[3], A. Elghali[4], F. Parat[1], J. Aubineau[1], J.-L. Bodinier[1,4]



https://doi.org/10.7185/geochemlet.2326

## Abstract

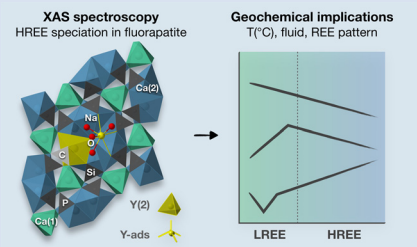


Fluorapatite (FAp), which occurs in various geological settings, contains rare earth elements (REE) for which unveiling the crystal chemistry is a key geochemical issue, especially for unravelling the conditions of fractionation and crystallisation. However, no consensus has been reached regarding their binding modes in FAp, with studies suggesting $REE^{3+}$-$Ca^{2+}$ substitution at the Ca(1) site, or at the Ca(2) site, or involving adsorption mechanisms. Our contribution here is based on yttrium K-edge X-ray absorption spectroscopy (XAS), performed on two genetically contrasting minerals: a hydrothermal FAp (from Durango, Mexico), and a sedimentary phosphorite (from Morocco). The results clearly show that Y substitutes for the Ca(2) site in both FAp. However, the spectral differences observed for the sedimentary FAp (B-type carbonated-FAp) suggest a sorption model that is either i) a mixture of Y-Ca(2) substitution and Y-adsorbed as an inner shell complex, or ii) Y-Ca(2) substitution along with carbonate groups replacing phosphate groups in the surrounding atomic shell. These models of yttrium sorption in FAp shed new light on the understanding of rare earth partitioning and enrichment processes, with major geochemical implications such as i) the identification of crystallising fluids and temperature in magmatic-hydrothermal settings, and ii) preservation of past seawater-porewater conditions in sedimentary settings.

Received 12 December 2022 | Accepted 12 July 2023 | Published 25 August 2023

## Introduction

Fluorapatite (FAp; $Ca_5(PO_4)_3F$) is an accessory mineral that hosts significant amounts of rare earth elements (REE, including yttrium) from ~200 to 20,000 ppm (Emsbo *et al.*, 2015), where Y exhibits similar behaviour to heavy rare earth elements (HREE, from Gd to Lu) and is therefore associated with them. For Earth Sciences, REE normalised patterns in FAp are proxies to i) reconstruct partitioning models and determine partition coefficients (Blundy and Wood, 2003), ii) identify the source fluids, their chemical composition and their REE complexation (Mackie and Young, 1973; Krneta *et al.*, 2018), iii) characterise the deposition/crystallisation conditions such as temperature, pH, redox (Chen *et al.*, 2002; Kocsis *et al.*, 2016), and iv) reveal the potential late diagenetic or hydrothermal alterations (Reynard *et al.*, 1999; Cherniak, 2000). The crystal chemistry of REE in FAp also controls its partitioning and normalised patterns (Blundy and Wood, 2003). In addition, it can potentially provide valuable insight into the crystallisation conditions such as temperature (Khudolozhkin *et al.*, 1973; Pan and Fleet, 2002 and references therein), fluids (Mackie and Young, 1973) or diffusion (Cherniak, 2000). However, determining the sorption models of REE is not systematically well constrained and is at the heart of many studies since FAp can potentially integrate REE in two distinct crystallographic Ca sites, namely the 9 fold coordinated Ca(1) and the 7 fold coordinated Ca(2) sites (Hughes *et al.*, 1991) (Fig. S-1a, b), and can also show nano-crystallinity typically observed in sedimentary deposits (Aubineau *et al.*, 2022) that may favour adsorption mechanisms and apparent no-fractionation behaviour (Reynard *et al.*, 1999). In order to maintain electroneutrality, each of the above sorption models may involve coupled substitutions such as (Pan and Fleet, 2002 and references therein):

$$REE^{3+} + Na^{+} = 2Ca^{2+} \quad \text{Eq. 1}$$

$$REE^{3+} + Si^{4+} = Ca^{2+} + P^{5+} \quad \text{Eq. 2}$$

$$REE^{3+} + O^{2-} = Ca^{2+} + F^{-} \quad \text{Eq. 3}$$

$$2REE^{3+} + \square_{vacancy} = 3Ca^{2+} \quad \text{Eq. 4}$$

In a study based on ligand type, Urusov and Khudolozhkin (1974) suggested that light (L)REE preferentially occupy the more covalent Ca(l) position, while HREE display preference for the more ionic Ca(2) position. Conversely, X-ray diffraction structure refinements on synthetic REE-doped FAp suggest that LREE are favoured in Ca(2) while HREE are favoured in Ca(1) (Hughes *et al.*, 1991; Fleet and Pan, 1995). Moreover, Borisov and Klevtśova (1963) have demonstrated that

1. Geosciences Montpellier, Université de Montpellier, CNRS, Montpellier, France
2. ESRF, European Synchrotron Radiation Facility, Grenoble, France
3. ILM, Institut Lumière Matière, Université Claude Bernard Lyon 1, Lyon, France
4. GSMI, Geology and Sustainable Mining Institute, Mohammed VI Polytechnic University, Ben Guerir, Morocco
* Corresponding author (Email: clement.bonnet02@etu.umontpellier.fr)

substitutions of both LREE and HREE for Ca occurred only at the Ca(2) site which was confirmed by EPR (Electron Paramagnetic Resonance) spectroscopy (Chen *et al.*, 2002). In natural marine environments, Kashiwabara *et al.* (2018) proposed that deep sea muds mostly trap REE by adsorption onto FAp crystals. Similarly, Reynard *et al.* (1999) conclude that the REE adsorption is likely to occur in the case of sedimentary/biogenic FAp.

To contribute to the understanding of the crystal chemistry of REE, and more specifically HREE in FAp and geochemical implications that follows, we propose a direct characterisation of the yttrium speciation (*i.e.* fixation modes, coupled substitutions and crystallographic preferences) using X-ray absorption spectroscopy (XAS) at the Y K-edge. XANES (X-ray absorption near edge structure) and EXAFS (extended absorption near edge structure) spectra are analysed by quantitative refinements, linear combinations and wavelet analysis (Muñoz *et al.*, 2003). This study focuses on two representative and genetically contrasting natural FAp: i) of hydrothermal origin (H-FAp) from Durango, Mexico, and ii) of sedimentary origin (S-FAp) from Moroccan phosphorites, and mainly composed of B-type carbonated FAp (*i.e.* FAp showing carbonate-phosphate substitutions).

## Yttrium Speciation in Model Compounds

Two model compounds, $Y_2O_3$ and synthetic Y-adsorbed FAp (Y-ads), were studied and used for qualitative and quantitative analysis of spectroscopic data. Their normalised XANES and EXAFS spectra show contrasting spectral signatures (Fig. 1a and b, respectively). For both compounds, the wavelet analysis of the EXAFS spectra (Fig. 2a and b, respectively) shows a maximum of the 1st neighbours' amplitude (*i.e.* $(R + \Phi) = 1.75$ Å) localised around 5.5 $Å^{-1}$. For $Y_2O_3$, the second and third shells are significantly shifted at higher *k* (wavenumber) values due to the presence of yttrium (Fig. 2a). However, the presence of oxygen in these shells moderates the shift of the amplitude term (maximum ~7.5 $Å^{-1}$), showing a strong asymmetric shape due to the distribution of Y, O and Y at distances of 3.53(4), 4.02(3) and 4.01(5) Å, respectively (Table 1).

Regarding Y-ads, the EXAFS shell fitting reveals the presence of 8.1(8) oxygen 1st neighbours located at 2.38(1) Å (Fig. 2b, Table 1), which is consistent for Y-adsorbed species (Ragnarsdottir *et al.*, 1998). Additionally, the best fit is obtained with two Ca as 2nd neighbours at 2.98(2) Å, suggesting a tridendate ionic bonding with the FAp crystal surface in the c axis channel. Note that in such a configuration (Fig. 3b), a typical O–Y–O angle of about 73°, characteristic of the regular 8 fold polyhedron, is preserved (Ni *et al.*, 1995). The 3rd shell observed on the wavelet modulus (Fig. 2b) shows a contribution at high *k* values (~8.5 $Å^{-1}$), which is in agreement with the presence of one Y fitted at 3.87(3) Å (Table 1). The latter probably results from Y pairs adsorbed on a single c axis channel, consistent with the formation of Y polyatomic species or Y polymerisation in water (Ragnarsdottir *et al.*, 1998).

## Yttrium Speciation in Hydrothermal Fluorapatite

The shell fitting performed on the EXAFS spectrum of hydrothermal FAp (H-FAp) reveals the presence of 7.0(7) oxygen located at 2.37(2) Å (Table 1), confirming that Y integrates the FAp crystal lattice within the 7 fold coordinated Ca(2) site by a substitution mechanism (hereafter referred to as Y(2); Fig. 3a). The fitted next nearest neighbour environment around Y, which consists of 5 P distributed between 3.09(1) and 3.70(1) Å, and 10 Ca at an average distance of 4.16(1) Å (Table 1), shows consistency with the theoretical Ca(2) atomic landscape (Tables 1, S-1b). In contrast, the radial distribution function around Ca(1) shows an intense peak in the Fourier transform (FT) magnitude (see *ab initio* EXAFS calculations and corresponding FT in Fig. S-2), due to the presence of 2 Ca located as close as 3.42 and 3.45 Å (Table S-1a). This feature appears strongly incompatible with the yttrium atomic landscape observed and successfully fitted in H-FAp (Fig. 2c, Table 1).

The lack of a high *k* contribution in the next nearest environment around Y eliminates the hypothesis of a coupled substitution involving a second heavy trivalent cation such as REE plus a vacancy (*i.e.* Eq. 4). Thus, the charge compensation is likely to meet the assumptions presented in Equations 1, 2 and 3, although these cannot be formally verified since the contrast in atomic number and coordination number (CN) between,

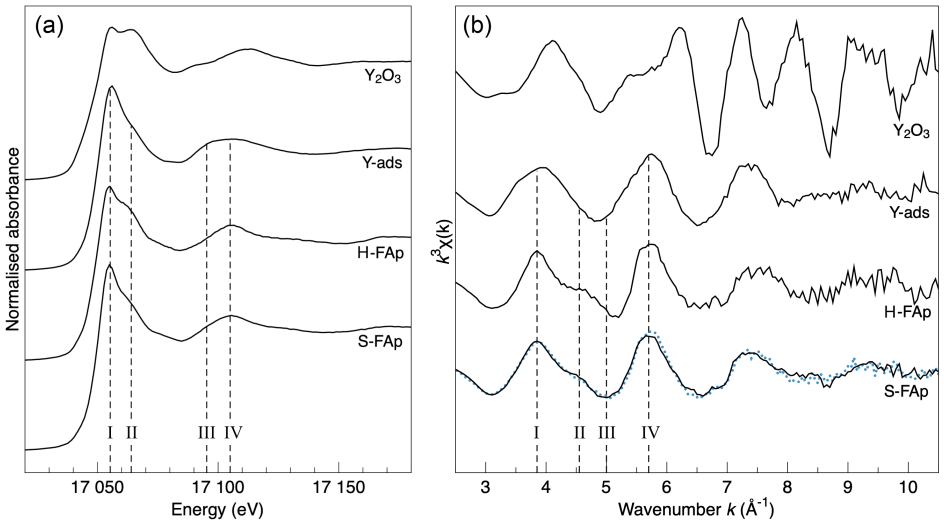


**Figure 1** X-ray absorption spectra collected at the Y K-edge for $Y_2O_3$ and Y-ads FAp model compounds, and H-FAp and S-FAp samples. **(a)** Normalised XANES spectra, **(b)** $k^3$-weighted EXAFS spectra. Roman numerals (I to IV) refer to characteristic spectral features. Blue dotted line represents the linear combination fit (LCF) result based on Y-ads and H-FAp components, suggesting a mixture of 59 % Y substituted at the Ca(2) site and 41 % of adsorbed Y for S-FAp.

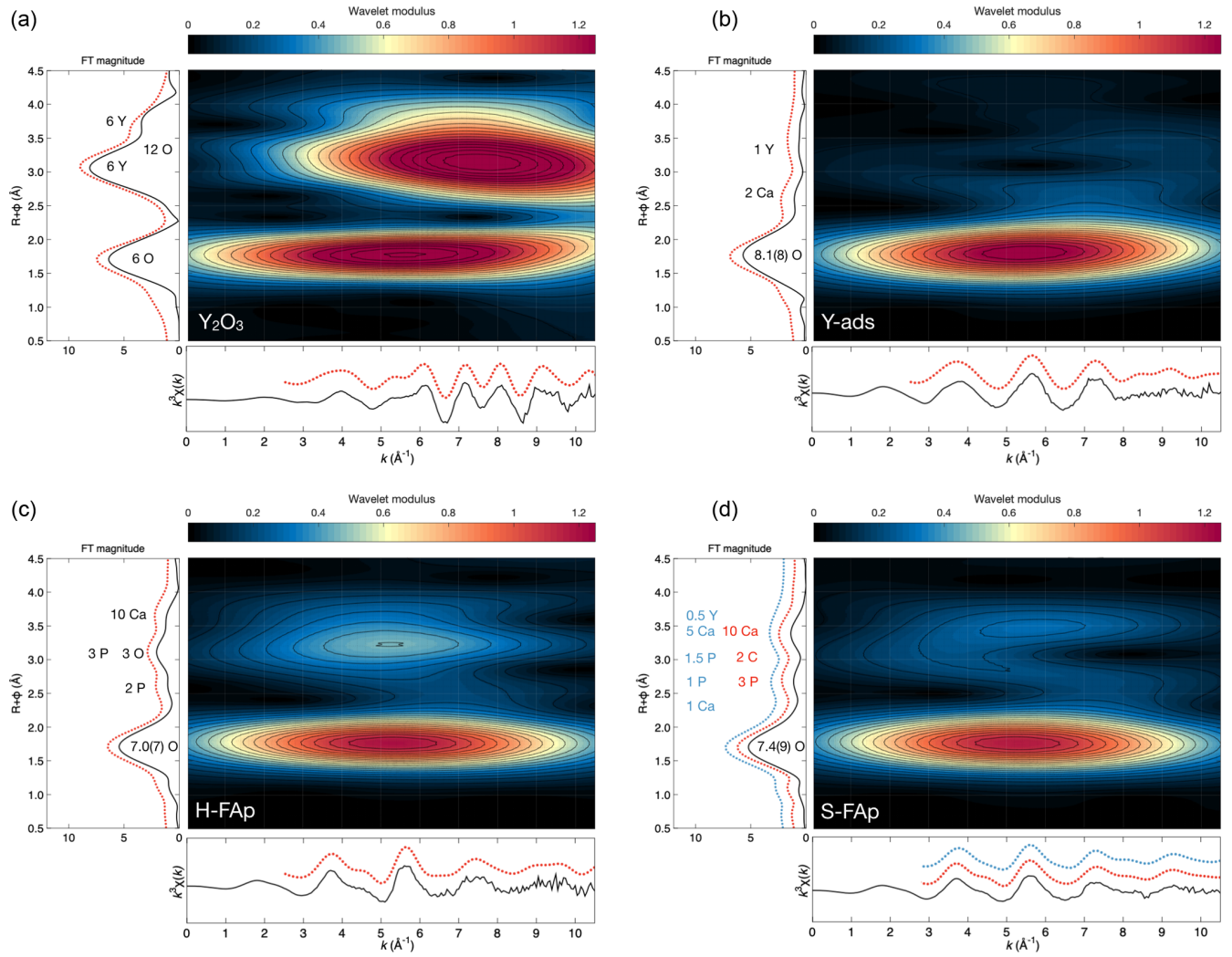


**Figure 2** Wavelet transform analysis of EXAFS spectra with corresponding $k^3$-weighted EXAFS spectra and Fourier transform (black solid lines). Results of multi-shell fits are shown in both the *k*-, and R-spaces (shifted dotted lines), **(a)** $Y_2O_3$, **(b)** Y-ads, **(c)** H-FAp, **(d)** S-FAp with the mixed "Y(2) + Y-ads" model in blue and the "Y(2) + carbonate" model in red.

respectively, Na and Ca, Si and P, and O and F are too subtle to be distinguished.

## Yttrium Speciation in Sedimentary Fluorapatite

The fit of the S-FAp EXAFS spectrum provides, for the 1st atomic shell, an average coordination of 7.4(9) (Table 1), which is slightly higher than that obtained for H-FAp, but within the margin of error. We also note on the wavelet modulus of S-FAp (Fig. 2d), a major difference in the 3rd neighbour shell, at $(R + \Phi) \approx 3.25$ Å (Fig. 2c), where a clear contribution arising from 3 P and 3 O (at 3.39 and 3.67 Å, respectively) is observed for H-FAp, but absent for S-FAp. To interpret these discrepancies, we propose two distinct structural models that were successfully fitted (Table 1, Fig. 2).

The first one (blue dotted lines in Fig. 2d) involves a mixture of two speciation models: a Y(2) substitution and an inner shell Y adsorption, the latter tending to decrease the intensity of the contribution located at $(R + \Phi) \approx 3.25$ Å. Note that a mixture with Y(1) results in a failed fit and is therefore excluded given the absence of its typical contribution of Ca located at ~3.43 Å (Figs. S-1a, S-2b, Table S-1a; $(R + \Phi) \approx 3$ Å in Fig. 2c and d). Additionally, different features of the XANES and EXAFS spectra tend to corroborate such a scenario (Fig. 1). Among them, the maximum of the white line (feature I in Fig. 1a) is significantly higher for Y-ads compared to H-FAp, while it shows an intermediate value for S-FAp. In accordance, the linear combination fit (LCF) of the EXAFS spectrum (Fig. 1b) also suggests a mixture of Y(2) and Y-ads.

The second model (red dotted lines in Fig. 2d) rather implies Y(2) together with two concomitant carbonate groups $(CO_3)^{2-}$ replacing two phosphate groups $(PO_4)^{3-}$ in the 3rd atomic shell. The presence of carbon in the neighbouring of yttrium causes the decrease in intensity of the $(R + \Phi) \approx 3.25$ Å contribution; light elements (C) having lower back scattering amplitudes than heavier elements (P). This model is in perfect agreement with i) the nature of S-FAp, which is identified as B-type carbonate-FAp (Figs. S-5, S-6), and ii) the location of structural carbonate groups, as determined by high resolution transmission electron microscopy on B-type carbonate-FAp (Kis *et al.*, 2019). Such a "Y(2) + carbonate" model implies a significant distortion of the crystal lattice (Table 1) and a co-location of C and REE, which is consistent with the results of Liao *et al.* (2019) in analogous samples. In this case, the excess

**Table 1** EXAFS fitting results for selected Y-standards and natural FAp samples and corresponding theoretical structural model. CN stands for the coordination number, R for the radial distance, $\sigma^2$ for the Debye-Waller factor and $\Delta c_3$ for the anharmonic parameter. The estimated parameters have uncertainty values in brackets, while fixed parameters do not. Linked estimated parameters share one of these superscript symbols: +, ++, *, **. Theoretical structures references: (1) Faucher and Pannetier (1980); (2) Ni *et al*. (1995); (3) Hughes *et al*. (1990).

| Fitted sample | Theoretical model of local structure applied to fit | | | | Multiple shell fitting | | | | Fit information and statistics | | |
|---|---|---|---|---|---|---|---|---|---|---|---|
| | Cluster | Path | CN | R (Å) | CN | R (Å) | $\sigma^2$ (Å$^{-2}$) | $\Delta c_3$ (Å$^{-3}$) | Fitted parameters | Degree of freedom | R-factor (%) |
| $Y_2O_3$ | $Y_2O_3$[(1)] | $Y\text{-}O_1$ | 6.0 | 2.28 | 6.0 | 2.30 (1) | 0.008 (2) | | 8 | 17 | 1.9 |
| | | $Y\text{-}Y_1$ | 6.0 | 3.55 | 6.0 | 3.54 (4) | 0.003 (1) | | | | |
| | | $Y\text{-}Y_2$ | 6.0 | 4.05 | 6.0 | 4.01 (5) | 0.004 (2) | | | | |
| | | $Y\text{-}O_{2,3}$ | 12.0 | 4.09 | 12.0 | 4.02 (3) | 0.009 (2) | | | | |
| Y-ads | Y adsorbed[(2,3)] | $Y\text{-}O_1$ | 8.0 | 2.38 | 8.1 (8) | 2.38 (1) | 0.008 (1) | 0.0007 (2) | 8 | 17 | 2.9 |
| | | $Y\text{-}Ca_1$ | 2.0 | 2.96 | 2.0 | 2.96 (2) | 0.011 (2) | | | | |
| | | $Y\text{-}Y_1$ | 1.0 | 3.87 | 1.0 | 3.87 (3) | 0.006 (3) | | | | |
| H-FAp | Ca(2)FAp[(3)] | $Y\text{-}O_1$ | 7.0 | 2.44 | 7.0 (7) | 2.37 (2) | 0.008 (1) | 0.0015 (4) | 10 | 17 | 0.95 |
| | | $Y\text{-}P_1$ | 1.0 | 3.08 | 1.0 | 3.09 (1)$^{+}$ | 0.002 (1)$^{*}$ | | | | |
| | | $Y\text{-}P_2$ | 1.0 | 3.26 | 1.0 | 3.28 (1)$^{+}$ | 0.002 (1)$^{*}$ | | | | |
| | | $Y\text{-}O_{2,3}$ | 3.0 | 3.35 | 3.0 | 3.40 (4)$^{++}$ | 0.015 (6)$^{**}$ | | | | |
| | | $Y\text{-}P_3$ | 1.0 | 3.49 | 1.0 | 3.51 (1)$^{+}$ | 0.002 (1)$^{*}$ | | | | |
| | | $Y\text{-}P_4$ | 2.0 | 3.68 | 2.0 | 3.70 (1)$^{+}$ | 0.002 (1)$^{*}$ | | | | |
| | | $Y\text{-}Ca_{1,2}$ | 10.0 | 4.03 | 10.0 | 4.16 (1) | 0.015 (1) | | | | |
| S-FAp (1st fit) | Ca(2)FAp[(3)]+ Y adsorbed[(2,3)] | $Y\text{-}O_1$ | 7.5 | 2.44 | 7.4 (9) | 2.38 (4) | 0.009 (2) | 0.0017 (7) | 10 | 17 | 1.3 |
| | | $Y\text{-}Ca_1$ | 1.0 | 2.96 | 1.0 | 2.98 (2) | 0.008 (3) | | | | |
| | | $Y\text{-}P_{1,2}$ | 1.0 | 3.17 | 1.0 | 3.16 (6)$^{+}$ | 0.006 (8)$^{*}$ | | | | |
| | | $Y\text{-}P_3$ | 0.5 | 3.49 | 0.5 | 3.49 (6)$^{+}$ | 0.006 (8)$^{*}$ | | | | |
| | | $Y\text{-}P_4$ | 1.0 | 3.68 | 1.0 | 3.68 (6)$^{+}$ | 0.006 (8)$^{*}$ | | | | |
| | | $Y\text{-}Y_1$ | 0.5 | 3.87 | 0.5 | 4.06 (2)$^{++}$ | 0.014 (3)$^{**}$ | | | | |
| | | $Y\text{-}Ca_{1,2}$ | 5.0 | 4.03 | 5.0 | 4.12 (2)$^{++}$ | 0.014 (3)$^{**}$ | | | | |
| S-FAp (2nd fit) | Ca(2) B-type FAp[(3)] | $Y\text{-}O_1$ | 7.0 | 2.44 | 7.4(9) | 2.38 (4) | 0.009 (2) | 0.0017 (7) | 11 | 17 | 0.4 |
| | | $Y\text{-}P_{1,2}$ | 2.0 | 3.17 | 2.0 | 3.14 (2)$^{+}$ | 0.008 (3)$^{*}$ | | | | |
| | | $Y\text{-}P_3$ | 1.0 | 3.49 | 1.0 | 3.36 (2)$^{+}$ | 0.008 (3)$^{*}$ | | | | |
| | | $Y\text{-}C_4$ | 2.0 | 3.68 | 2.0 | 3.47 (4) | 0.005 (7) | | | | |
| | | $Y\text{-}Ca_{1,2}$ | 10.0 | 4.03 | 10.0 | 4.24 (6) | 0.019 (3) | 0.0023 (9) | | | |

of charge of $Y^{3+}$ could be balanced according to the following equations:

$$Y^{3+} + \square_{vacancy} + Na^{+} + 2CO_3^{2-} = 3Ca^{2+} + 2PO_4^{3-} \quad \text{Eq. 5}$$

$$Y^{3+} + \square_{vacancy} + 2CO_3^{2-} + O^{2-} = 2Ca^{2+} + 2PO_4^{3-} + F^{-} \quad \text{Eq. 6}$$

where the vacancies likely refer to Ca(2) sites, and sodium, fluorine or carbonates are most often in excess relative to rare earth elements. However, it is not possible to formally distinguish these two hypotheses using the approach proposed here, and further *in situ* characterisation at the micrometric scale is required.

## Geochemical Implications

In accordance with the crystal lattice strain partitioning model, it is proposed that the partition coefficient of REE in magmatic-hydrothermal FAp originates from the crystallographic preference of HREE for the Ca(1) site, and LREE for the Ca(2) site (Hughes *et al.*, 1991). However, in the case of Durango FAp, we clearly point out that Y substitutes for Ca in the Ca(2) site. This could suggest that a partition model involving the Ca(1) site for HREE is not appropriate for the Durango FAp, where a HREE-depleted normalised pattern (Fleet and Pan, 1995) could rather reflect the progressive ionic incompatibility of REE for the Ca(2) site along the lanthanide series. These assumptions should be taken with caution given that the Durango FAp does not prevail for all other FAp, and given that REE patterns may vary significantly depending on the fluid conditions (Krneta *et al.*, 2018). Indeed, it is possible that the Durango H-FAp undergoes geochemical processes that favour Ca(2), as diffusion of REE in the Ca(2) site through the c axis channel may occur during thermal events (Cherniak, 2000). Furthermore, the different complexation modes in solution play a role in the distribution of REE between Ca(2) and Ca(1) sites involving Na or Si coupled substitutions (Mackie and Young, 1973). For example, the preference of REE for Ca(2) decreases with increasing Si content or temperature in the 700–1200 °C range (Khudolozhkin *et al.*, 1973; Pan and Fleet, 2002 and references therein). This could confirm that the Durango FAp was more likely formed at a medium temperature with saline fluids, in agreement with the literature (Gleason *et al.*, 2000 and references therein).

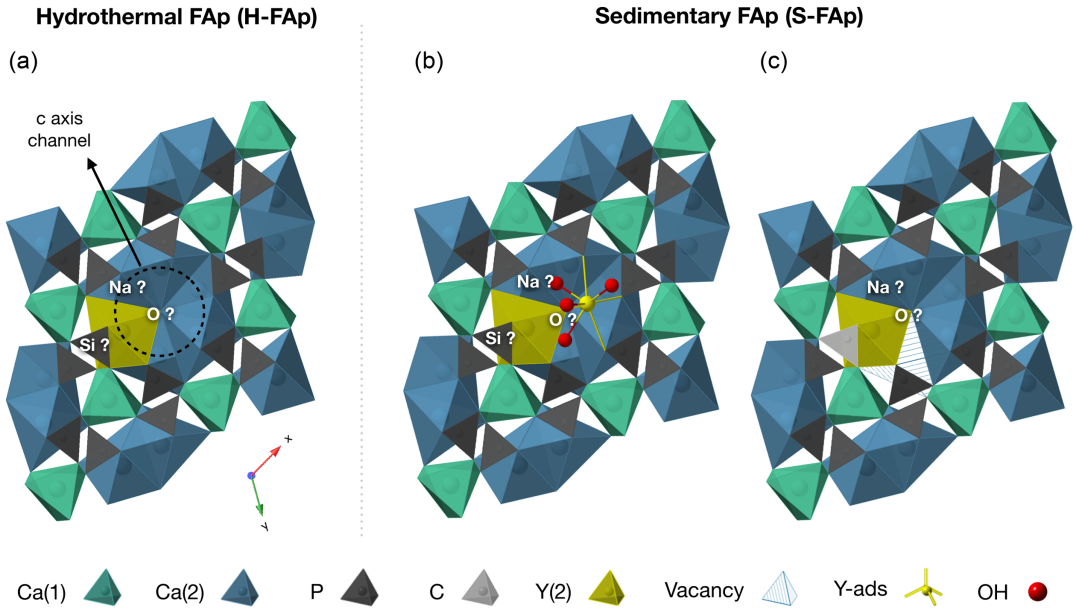


**Figure 3** Fluorapatite crystal structure projected along c axis showing yttrium speciation models, **(a)** H-FAp: substitution at the Ca(2) site, **(b)** S-FAp: mixture of substitution at the Ca(2) site together with an inner shell adsorption at the c axis channel, **(c)** S-FAp: substitution at the Ca(2) site with concomitant C replacing P and Ca vacancy. Si, Na and O labels indicate potential coupled substitutions required to compensate the excess of electronic charge due to $Y^{3+}$-$Ca^{2+}$ substitution.

In this perspective, systematic *in situ* X-ray absorption studies of REE on other natural FAp could provide more information on the hydrothermal-magmatic fluids or be used as a geothermometer, which could lead to a major re-interpretation of geochemical processes and crystallisation conditions (Krneta *et al.*, 2018). This could also make it possible to decipher the effect of extrinsic (*e.g.*, temperature, source fluids) and intrinsic (*e.g.*, crystal-chemical) variables on REE patterns (Rakovan *et al.*, 2001; Borst *et al.*, 2020).

For sedimentary FAp, the assumptions for Y speciation, which include either mixed "Y(2) + Y-ads" speciation or the "Y(2) + carbonates" speciation, are both compatible with an adsorption-diffusion-substitution process (Koeppenkastrop and de Carlo, 1992). Both models can explain why REE in carbonated-FAp show a normalised pattern without fractionation, characterised by HREE enrichment so-called "past seawater pattern" (Reynard *et al.*, 1999). The Y(2) + carbonate model is particularly relevant because REE are mainly complexed by carbonate groups in seawater, which also shows a HREE-enriched pattern (Schijf and Byrne, 2021). We thus assume that the conservative (*i.e.* without fractionation) REE uptake in FAp is likely to be promoted by carbonate complexation, where both REE and carbonates are trapped in the FAp lattice during early diagenesis by their direct uptake from the hydrated layer (Cazalbou *et al.*, 2004). Since REE and carbonates are mainly enriched concomitantly in a strongly distorted crystal fringe located in the outer edges of FAp nanocrystallites (Liao *et al.*, 2019; in agreement with our EXAFS results), the crystal chemistry effect on the partitioning is inhibited while the effect of the fluid complexation (*i.e.* REE carbonate ions in seawater or porewater) is predominantly recorded, which likely implies non-Henry's Law behaviour for the REE partitioning in S-FAp (Pan *et al.*, 2003).

Therefore, *in situ* X-ray absorption studies of REE could be applied to marine geochemistry to estimate whether overprinting of REE FAp fractionation has occurred, and whether a reliable seawater-porewater signature is preserved. This is particularly valuable for examining temporally laminated structures containing FAp, such as phosphorite grains or some polymetallic nodules, used to unravel past seawater conditions and their temporal changes like pH, redox, or ocean circulation (Kocsis *et al.*, 2016).

## Conclusions

We studied the speciation of yttrium, a geochemical proxy for HREE, in hydrothermal and sedimentary FAp minerals using X-ray absorption spectroscopy. Analyses of Y K-edge XANES and EXAFS spectra, including *ab initio* calculations, shell fitting, wavelet analysis and linear combination show that:

1) Y exclusively substitutes for Ca in the Ca(2) site in the hydrothermal Durango FAp;
2) Y can be found either as a mixture of Ca(2) substituted and inner shell tridentate adsorbate in the c axis channel in sedimentary FAp, or as substitution for the Ca(2) site with coupled substitution of a carbonate group in the direct surrounding atomic environment in B-type carbonated FAp.

Regardless of the FAp origin, the charge compensation mechanism is likely to be based on coupled substitutions such as:

$$Y^{3+} + Na^{+} = 2Ca^{2+}$$

$$Y^{3+} + Si^{4+} = Ca^{2+} + P^{5+}$$

$$Y^{3+} + O^{2-} = Ca^{2+} + F^{-}$$

Although the latter substitutions were not distinguished by our approach, we excluded the $2Y^{3+} + \square_{vacancy} = 3Ca^{2+}$ substitution due to the failure to detect Y or other heavy elements in the nearest atomic shell around Y.

For the sedimentary B-type carbonated FAp, we suggest that the following substitutions are likely to occur:

$$Y^{3+} + \square_{vacancy} + Na^{+} + 2CO_3^{2-} = 3Ca^{2+} + 2PO_4^{3-}$$

$$Y^{3+} + \square_{vacancy} + 2CO_3^{2-} + O^{2-} = 2Ca^{2+} + 2PO_4^{3-} + F^{-}$$

Regardless of geological context, Y speciation provides crucial information for a better understanding of REE partitioning and the geochemical information derived from it.

## Acknowledgments

Work carried out within the framework of the scientific cooperation agreement between the Mohammed VI Polytechnic University, the University of Montpellier and the Centre National de la Recherche Scientifique [Specific Agreement n°UM190775 on "The multi-scale distribution of minor and trace elements in Moroccan phosphate basins"]. We also acknowledge the European Synchrotron Radiation Facility for provision of synchrotron radiation facilities. We thank Bernard Fraisse for his technical assistance with the XRD measurements at the RRXG platform (Réseau des Rayons X et Gamma) of University of Montpellier (Montpellier, France). We would also like to thank Valérie Magnin for her contribution to the micro-XRF data carried out at the ISTerre laboratory (Grenoble, France).

*Editor: Satish Myneni*

## Author Contributions

JLB and AE participated in the sediment sampling strategy. VMR carried out the acquisition and processing of the LIBS data. JA provided FTIR measurements. CB carried out the XRF and XRD measurements. CB, MM and OM performed XANES and EXAFS acquisitions which were then processed by CB and MM. CB and MM wrote the manuscript. All authors participated to discussions.

## Additional Information

**Supplementary Information** accompanies this letter at https://www.geochemicalperspectivesletters.org/article2326.



**Cite this letter as:** Bonnet, C., Muñoz, M., Mathon, O., Motto-Ros, V., Elghali, A., Parat, F., Aubineau, J., Bodinier, J.-L. (2023) Sorption model for yttrium in fluorapatite: Geochemical implications. *Geochem. Persp. Let.* 27, 1–7. https://doi.org/10.7185/geochemlet.2326

## References

Aubineau, J., Parat, F., Elghali, A., Raji, O., Addou, A., Bonnet, C., Muñoz, M., Mauguin, O., Baron, F., Jouti, M.B., Yazamid, O.K., Bodinier, J.-L. (2022) Highly variable content of fluorapatite-hosted $CO_3^{2-}$ in the Upper Cretaceous/ Paleogene phosphorites (Morocco) and implications for paleodepositional conditions. *Chemical Geology* 597, 120818. https://doi.org/10.1016/j.chemgeo.2022.120818

Blundy, J., Wood, B. (2003) Partitioning of trace elements between crystals and melts. *Earth and Planetary Science Letters* 210, 383–397. https://doi.org/10.1016/S0012-821X(03)00129-8

Borisov, S.V., Klevtśova, R.F. (1963) The crystal structure of TR-Sr-apatite. *Journal of Structural Chemistry* 4, 575–577. https://doi.org/10.1007/BF00747639

Borst, A.M., Finch, A.A., Friis, H., Horsburgh, N.J., Gamaletsos, P.N., Goettlicher, J., Steininger, R., Geraki, K. (2020) Structural state of rare earth elements in eudialyte-group minerals. *Mineralogical Magazine* 84, 19–34. https://doi.org/10.1180/mgm.2019.50

Cazalbou, S., Eichert, D., Drouet, C., Combes, C., Rey, C. (2004) Minéralisations biologiques à base de phosphate de calcium. *Comptes Rendus Palevol* 3, 563–572. https://doi.org/10.1016/j.crpv.2004.07.003

Chen, N., Pan, Y., Weil, J.A. (2002) Electron paramagnetic resonance spectroscopic study of synthetic fluorapatite: Part I. Local structural environment and substitution mechanism of $Gd^{3+}$ at the Ca2 site. *American Mineralogist* 87, 37–46. https://doi.org/10.2138/am-2002-0105

Cherniak, D.J. (2000) Rare earth element diffusion in apatite. *Geochimica et Cosmochimica Acta* 64, 3871–3885. https://doi.org/10.1016/S0016-7037(00)00467-1

Emsbo, P., McLaughlin, P.I., Breit, G.N., du Bray, E.A., Koenig, A.E. (2015) Rare earth elements in sedimentary phosphate deposits: Solution to the global REE crisis? *Gondwana Research* 27, 776–785. https://doi.org/10.1016/j.gr.2014.10.008

Faucher, M., Pannetier, J. (1980) Refinement of the $Y_2O_3$ structure at 77 K. *Acta Crystallographica Section B* 36, 3209–3211. https://doi.org/10.1107/S0567740880011351

Fleet, M.E., Pan, Y. (1995) Site preference of rare earth elements in fluorapatite. *American Mineralogist* 80, 329–335. https://doi.org/10.2138/am-1995-3-414

Gleason, J.D., Marikos, M.A., Barton, M.D., Johnson, D.A. (2000) Neodymium isotopic study of rare earth element sources and mobility in hydrothermal Fe oxide (Fe-P-REE) systems. *Geochimica et Cosmochimica Acta* 64, 1059–1068. https://doi.org/10.1016/S0016-7037(99)00325-7

Hughes, J.M., Cameron, M., Crowley, K.D. (1990) Crystal structures of natural ternary apatites: Solid solution in the $Ca_5(PO_4)_3X$ (X = F, OH, Cl) system. *American Mineralogist* 75, 295–304. http://www.minsocam.org/ammin/AM75/AM75_295.pdf

Hughes, J.M., Cameron, M., Mariano, A.N. (1991) Rare-earth-element ordering and structural variations in natural rare-earth-bearing apatites. *American Mineralogist* 76, 1165–1173. http://www.minsocam.org/ammin/AM76/AM76_1165.pdf

Kashiwabara, T., Toda, R., Nakamura, K., Yasukawa, K., Fujinaga, K., Kubo, S., Nozaki, T., Takahashi, Y., Suzuki, K., Kato, Y. (2018) Synchrotron X-ray spectroscopic perspective on the formation mechanism of REY-rich muds in the Pacific Ocean. *Geochimica et Cosmochimica Acta* 240, 274–292. https://doi.org/10.1016/j.gca.2018.08.013

Khudolozhkin, V.O., Urusov, V.S., Tobelko, K.I., Vernadskiy, V.I. (1973) Dependence of structural ordering of rare earth atoms in the isomorphous series apatite-britholite (abukumalite) on composition and temperature. *Geochemical International* 10, 1171–1177.

Kis, V.K., Czigány, Z., Dallos, Z., Nagy, D., Dódony, I. (2019) HRTEM study of individual bone apatite nanocrystals reveals symmetry reduction with respect to $P6_3/m$ apatite. *Materials Science and Engineering: C* 104, 109966. https://doi.org/10.1016/j.msec.2019.109966

Kocsis, L., Gheerbrant, E., Mouflih, M., Cappetta, H., Ulianov, A., Chiaradia, M., Bardet, N. (2016) Gradual changes in upwelled seawater conditions (redox, pH) from the late Cretaceous through early Paleogene at the northwest coast of Africa: Negative Ce anomaly trend recorded in fossil bio-apatite. *Chemical Geology* 421, 44–54. https://doi.org/10.1016/j.chemgeo.2015.12.001

Koeppenkastrop, D., de Carlo, E.H. (1992) Sorption of rare-earth elements from seawater onto synthetic mineral particles: An experimental approach. *Chemical Geology* 95, 251–263. https://doi.org/10.1016/0009-2541(92)90015-W

Krneta, S., Ciobanu, C.L., Cook, N.J., Ehrig, K.J. (2018) Numerical Modeling of REE Fractionation Patterns in Fluorapatite from the Olympic Dam Deposit (South Australia). *Minerals* 8, 342. https://doi.org/10.3390/min8080342

Liao, J., Suna, X., Li, D., Sae, R., Lub, Y., Lin, Z., Xub, L., Zhanf, R., Pang, Y., Xuh, H. (2019) New insights into nanostructure and geochemistry of bioapatite in REE-rich deep-sea sediments: LA-ICP-MS, TEM, and Z-contrast imaging studies. *Chemical Geology* 512, 58–68. https://doi.org/10.1016/j.chemgeo.2019.02.039

Mackie, P.E., Young, R.A. (1973) Location of Nd dopant in fluorapatite, $Ca_5(PO_4)_3F$: Nd. *Journal of Applied Crystallography* 6, 26–31. https://doi.org/10.1107/S0021889873008009

Muñoz, M., Argoul, P., Farges, F. (2003) Continuous Cauchy wavelet transform analyses of EXAFS spectra: A qualitative approach. *American Mineralogist* 88, 694–700. https://doi.org/10.2138/am-2003-0423

Ni, Y., Hughes, J.M., Mariano, A.N. (1995) Crystal chemistry of the monazite and xenotime structures. *American Mineralogist* 80, 21–26. https://doi.org/10.2138/am-1995-1-203

Pan, Y., Fleet, M.E. (2002) Compositions of the Apatite-Group Minerals: Substitution Mechanisms and Controlling Factors. *Reviews in Mineralogy and Geochemistry* 48, 13–49. https://doi.org/10.2138/rmg.2002.48.2

Pan, Y., Dong, P., Chen, N. (2003) Non-Henry's Law behavior of REE partitioning between fluorapatite and $CaF_2$-rich melts: Controls of intrinsic vacancies and implications for natural apatites. *Geochimica et Cosmochimica Acta* 67, 1889–1900. https://doi.org/10.1016/S0016-7037(02)01285-1

Ragnarsdottir, K.V., Oelkers, E.H., Sherman, D.M., Collins, C.R. (1998) Aqueous speciation of yttrium at temperatures from 25 to 340°C at $P_{sat}$: an in situ EXAFS study. *Chemical Geology* 151, 29–39. https://doi.org/10.1016/S0009-2541(98)00068-0

Rakovan, J., Newville, M., Sutton, S. (2001) Evidence of heterovalent europium in zoned Llallgua apatite using wavelength dispersive XANES. *American Mineralogist* 86, 697–700. https://doi.org/10.2138/am-2001-5-610

Reynard, B., Lécuyer, C., Grandjean, P. (1999) Crystal-chemical controls on rare-earth element concentrations in fossil biogenic apatites and implications for paleoenvironmental reconstructions. *Chemical Geology* 155, 233–241. https://doi.org/10.1016/S0009-2541(98)00169-7

Schijf, J., Byrne, R.H. (2021) Speciation of yttrium and the rare earth elements in seawater: Review of a 20-year analytical journey. *Chemical Geology* 584, 120479. https://doi.org/10.1016/j.chemgeo.2021.120479

Urusov, V.S., Khudolozhkin, V.O. (1974) An energy analysis of cation ordering in apatite. *Geochemistry International* 11, 1048–1053.

Geochemical Perspectives Letters



# Sorption model for yttrium in fluorapatite: Geochemical implications

**C. Bonnet, M. Muñoz, O. Mathon, V. Motto-Ros, A. Elghali, F. Parat, J. Aubineau, J-L. Bodinier**

The Supplementary Information includes:



## 1. Samples and Model Compounds

### 1.1. Natural Fluorapatite Samples

Two natural fluorapatite (FAp) samples were studied. The first sample is a pure hydrothermal fluorapatite monocrystal (hereafter referred to as H-FAp) from Cerro de Mercado, Durango, Mexico. This FAp sample is associated with felsic volcanic rocks (Lyons, 1988), where the abundance of hydrothermal features, as well as many geochemical similarities to other similar types of Fe-P-REE deposits suggest a paragenetically late hydrothermal origin (Gleason *et al.*, 2000). Durango FAp is a standard reference fluorapatite material for mineralogy, geochemistry, and thermochronology (*e.g.*, Chew *et al.*, 2014). The Y content of this sample is 888 ppm (Fig. S-3).

The second sample consists of a sedimentary phosphorus (P)-rich deposit (*i.e.* phosphorite) from Morocco (El Bamiki *et al.*, 2021). This sample was first characterised by X-ray diffraction (XRD) on whole-rock powder to determine the mineral paragenesis. Based on semi-quantitative Rietveld refinement, the sample contains ~89.2 wt. % of FAp as well as 6.2 wt. % quartz and 4.6 wt. % carbonates (Fig. S-4). The phosphorite-hosted FAp is often referred to as B-type carbonate fluorapatite (S-FAp) or "francolite" because of the significant incorporation of carbonate anions ($CO_3^{2-}$) into the structure in substitution for phosphate groups (Regnier *et al.*, 1994). The FTIR characterisation of the sample confirms that the sedimentary sample consists of a B-type carbonate FAp (Fig. S-5). Using the semi-quantification method of (Schuffert *et al.*, 1990), which rely on the XRD shifts of the (004) and (410) reflections, we estimate the amount of $CO_3^{2-}$ to be 8.26(13) % for the S-FAp sample (Fig. S-6). The Y concentration in this phosphorite is 332 ppm (Fig. S-3), dominantly hosted in S-FAp as shown by LIBS (laser induced breakdown spectroscopy) elemental maps (Fig. S-7) and corresponding correlation density plots (Fig. S-8).

In FAp minerals, REEs are likely to substitute for Ca, which is inequivalently distributed in two distinct crystallographic sites, namely Ca(1) and Ca(2). The Ca(1) crystallographic site displays a coordination number of 6 + 3, with 6 bonded oxygen atoms and 3 unbonded oxygens in a distorted tricapped trigonal prism geometry (Fig. S-1a; Hughes *et al.*, 1990). The first 6 oxygens are located at a mean distance of 2.43 Å, while the three most distant oxygens are found at a mean distance of 2.81 Å. Considering the coordination numbers 6 + 3, the overall mean distance is ~2.554 Å. Details regarding the location of the next 2$^{nd}$ and 3$^{rd}$ neighbours around the Ca(1) site are shown in Table S-1a. The Ca(2) crystallographic site shows a coordination number of 7, with 6 oxygen and 1 fluorine atoms, bonded in a distorted pentagonal bipyramid geometry (Fig. S-1b; Hughes *et al.*, 1990). The interatomic distances are distributed from 2.31 Å to 2.70 Å, with mean distance of 2.440 Å. The next 2$^{nd}$ and 3$^{rd}$ neighbour distances from the refined FAp structure of Hughes *et al.* (1990) are shown in Table S-1b.

### 1.2. Model Compounds

Two yttrium-rich model compounds have been selected for this study. First, yttrium oxide ($Y_2O_3$), also named yttria, have been purchased from Sigma Aldrich with a 99.99 % purity. $Y_2O_3$ crystallises in a cubic space group and presents two inequivalent $Y^{3+}$ sites (Faucher and Pannetier, 1980). In the first site, Y is bonded to 6 oxygen atoms that are distributed at Y-O bond distances ranging from 2.24 to 2.33 Å, with an average Y-O distance of 2.28 Å. In the second Y-site, yttrium is also bonded to 6 oxygen atoms all located at fixed Y-O distance of 2.29 Å. Due to its rather simple Y speciation including coordination number of 6 and an average Y-O distance of 2.285 Å, this model compound is mainly used here to fit the contributions of the first neighbouring oxygen atoms in the EXAFS spectra.

The second model compound consists of synthetic sample in which yttrium is adsorbed at the surface of a natural magmatic fluorapatite sample (referred to as Y-ads in the article). The Y content in the natural FAp is shown to be negligible compared to that of Y-ads (Fig. S-3). The synthesis follows the protocol of Kashiwabara *et al.* (2018) by adding a 50 mL solution of 0.50 mM $YCl_3 \cdot 6H_2O$ (from Sigma Aldrich) to 100 mg of the FAp powder. The ionic strength was set to 0.70 M (NaCl), and the pH was adjusted to 6.0 with HCl solution. After 24 h of equilibration in a magnetic stirring bath at 25 °C, suspensions were filtered with a membrane of 0.2 µm pore size using a vacuum pump. The solid phase was then thoroughly rinsed several times with Milli-Q water to remove the background solution (*i.e.* aqueous $YCl_3$). For this sample, the adsorbed Y is most likely 8-fold coordinated, which is consistent with the coordination number of ~8 found for Y adsorbed onto kaolinite (Borst *et al.*, 2020).

# 2. Analytical Methods

## 2.1. X-ray Fluorescence (XRF)

X-ray fluorescence measurements (Fig. S-3) were performed at the Geochemistry-Mineralogy platform of ISTerre (University of Grenoble, France). XRF spectra were collected for the model compounds as well as for natural samples using an EDAX EAGLE III µ-fluorescence X-ray probe with a Rh radiation source operating at 40 kV and 100 µA with a focal spot of 300 µm and a vacuum of 40 mbar. Acquisition time for each spectrum was set to 15 min corrected for deadtime. The Y content of the Y-ads model compound was estimated from a linear calibration curve based on H-FAp analysis by ICP-MS.

## 2.2. X-ray Diffraction (XRD)

Powder X-ray diffraction was used to characterise bulk mineralogy assemblage of the Moroccan phosphorite sample (Fig. S-4). The analysis was performed at the RRXG platform (Réseau des Rayons X et Gamma; ICGM, University of Montpellier, France). The diffraction pattern was recorded using a PANalytical X'Pert PRO MPD X-ray diffractometer with a Cu $K\alpha_1$ radiation source ($\lambda$ = 1.541 Å), at 45 kV and 20 mA with an angular range of 5°–70° 2$\theta$ and a step size of 0.02° 2$\theta$ per 2 s. Background subtraction, indexing of peaks, mineral identification and Rietveld refinement were processed using the *Profex-BGMN* software (Döbelin and Kleeberg, 2015). Semi-quantitative mineral abundance (Fig. S-4) was based on the following reference structures: fluorapatite (Hughes *et al*., 1990), calcite and dolomite (Graf, 1961), and quartz (Levien *et al*., 1980).

## 2.3. Laser Induced Breakdown Spectroscopy (LIBS)

Laser induced breakdown spectroscopy (LIBS) imaging (Cáceres *et al*., 2017; Motto-Ros *et al*., 2020), was used to perform major and trace elemental mapping on S-FAp prepared as thin section (Fig. S-7). The mapping area is 9 by 16 mm. The acquisition was based on a 1064 nm Nd:YAG laser, with a pulse of 700 µJ and 8 ns duration coupled to a 100 Hz repetition rate (Centurion, Lumibird, France) focused using a 15× magnification lens (LMM-15X-P01, Thorlabs, Germany). The plasma emission was collected by three lens-fibre systems coupled to three spectrometers, the Shamrock 303, the Shamrock 500, and the Avantes compact that, respectively, measure the wavelengths ranging from 210–240 nm (that includes P and Si lines), 350–390 nm (that includes Ca, Mg and Y lines), and 650–960 nm (that includes O line). The thin section was placed on an XYZ stage and scanned pixel-by-pixel with a lateral resolution of 18 µm. All experiments were conducted at 25 °C and 1 bar with an argon flow of 1.2 L/min through the plasma to both enhance the emission signal and prevent surface of ablated material contamination. For the data images, *LasMap* software (more details in Motto-Ros *et al*., 2020) was used to define a baseline, extract the line intensities (associated with the elements of interest) and reconstruct the elemental images.

LIBS images are used to produce correlation density plots showing a clear correlation between Y and FAp, while anti-correlations are observed between Y and carbonates, Y and quartz, and FAp and carbonates (Fig. S-8), demonstrating that Y is primarily hosted by FAp in this phosphorite sample.

## 2.4. Fourier Transform Infrared Spectroscopy (FTIR)

Fourier transform infrared (FTIR) spectra were acquired using a Nicolet iS50 FTIR spectrometer equipped with a potassium bromide (KBr) beamsplitter and a DTGS KBr detector at the IC2MP, University of Poitiers, France. Spectra were acquired in transmission mode from KBr pellets that consist of a mixture of 1 mg of sample and 149 mg of KBr. The mixture was then pressed for 5 min at 8 kbar and dried for more than 2 h in an oven at 120 °C. An accumulation of

100 scans at a resolution of 4 $cm^{-1}$ composes each spectrum. FTIR analyses in the 1600–400 $cm^{-1}$ region (middle infrared, MIR) were performed to further study the sedimentary sample, especially, the $CO_3^{2-}$ substitutions in FAp.

## 2.5. X-ray Absorption Spectroscopy (XAS)

***2.5.1. XAS pellets.*** Each sample was previously ground in a sterile agate mortar without water to a particle size <20 µm. The two fluorapatite samples were directly pressed to form 50 mg pellets with a diameter of 5 mm, which is suitable for XANES (X-ray absorption near edge structure) and EXAFS (extended X-ray absorption fine structure) large beam measurements in fluorescence mode. To avoid self-absorption effects due to high concentration of the absorbing atom, the reference compounds were diluted to 0.8 wt. % $Y_2O_3$ and 15 wt. % Y-ads into 98.2 and 85 wt. % cellulose, respectively, before pressing the mixtures into 50 mg pellets.

***2.5.2. Data acquisition.*** X-ray absorption spectroscopy measurements were performed at the ESRF (European Synchrotron Radiation Facility; Grenoble, France) using the BM23 beamline (Mathon *et al.*, 2015). The storage ring operating conditions were 6 GeV and 195 mA in the "Hybrid" injection mode. The source is a bending magnet two-poles wiggler monochromatised using a Si(111) double crystal monochromator (to maximise the photons flux). The incident beam was collimated at 2.5 × 1 mm. Measurements were collected in fluorescence mode at room temperature using a silicon drift Vortex detector located at 90° of the incident beam. The incidence angle was set to 45° for the "diluted" FAp samples to maximise detection, while it was set to 1° for the Y-rich model compounds to limit self-absorption effects. Energy calibration was ensured thanks to the simultaneous measurement of a Y-metal foil in transmission mode. The energy range was set to measure the Y K-edge (17,038 eV) absorption spectra in the XANES region (from 16,950 eV to 17,200 eV) as well as in the EXAFS region (from 17,100 eV to 17,600 eV).

***2.5.3. XANES and EXAFS data reduction.*** Raw data were first processed using the Athena software Demeter Perl packages (Ravel and Newville, 2005). XANES and EXAFS spectra were normalised to the X-ray source intensity (I0), while the absorption edge (E0) was set to the maximum of the first derivative (17,050 eV). EXAFS background was removed using the implemented AUTOBK background subtraction algorithm (Newville, 2001), using a spline ranging from 0 to 10.5 $Å^{-1}$ of $k^3$ weight with a Rbkg value of 1.1. Then, the Fourier transform was calculated from 2.5 to 10.5 $Å^{-1}$ in $k^3$ weight with a Hanning apodisation window and Hannnig coefficient of 3.

***2.5.4. Wavelet analysis.*** Continuous Cauchy wavelet transform analysis (Muñoz *et al.*, 2003) was first used to visualised the EXAFS spectra in three-dimensions: the wavevector ($k$), the interatomic distance uncorrected for phase-shifts (R + Φ), and the wavelet modulus (corresponding to the continuous decomposition of the EXAFS amplitude terms). The algorithm has been improved so that a constant resolution in ($k$) and (R + Φ) spaces was used, with respective values of 2 $Å^{-1}$ and 0.126 Å. This method provides straightforward qualitative information concerning the $k$-range of each EXAFS contribution, along the relative distances to the photoabsorber atom, to better assess the nearest-neighbours identification (depending on the shape of the backscattering amplitude and the intensity of the modulus). Furthermore, wavelet analysis constitutes a robust first step to the further multi-shell fits.

***2.5.5. Linear combination fit (LCF).*** EXAFS linear combination fit to identify a mixed speciation was carried out using the Athena software in a selected $k$-range from 2 to 8 $Å^{-1}$ (Fig. S-9). We selected both the Y-ads and H-FAp as main components to perform the linear combination fit of the S-FAp spectrum. All components share the same E0 (at 17,048 eV), and the fit result was forced to 1.

***2.5.6. EXAFS and Fourier transform multi-shell fit.*** EXAFS spectra and corresponding Fourier transform were fitted using the Artemis software (Ravel and Newville, 2005). The first atomic shell was first fitted individually on the basis of the backscatter amplitude and phase shift determined from the Y-O atomic pair of the crystalline $Y_2O_3$ model compound. The fitting of the first atomic shell was carried out by considering an anharmonic parameter (3rd order cumulant; $\Delta C_3$) to take into account site distortions and distance distribution in the coordination polyhedra. Then, the multi-shell fits were constrained based on the observations from the wavelet and LCF analyses. The EXAFS spectrum of H-FAp was successfully fitted on the basis of the atomic environment of the Ca(2) site, while the EXAFS spectrum of S-FAp was fitted on the basis of i) a mixture between the atomic environments of Y-ads and the Ca(2) site, and ii)

the atomic environment of the Ca(2) site with some C replacing P. All the multi-shell fits were processed in R-space between 1.1 and 4.5 Å with a fixed E0 value of 0 and a fixed amplitude factor value of 0.9 determined on the basis of the measurement of $Y_2O_3$ reference. The R-factor (%) represents the weighted mean squared deviation and the error in % between the data and the corresponding fit. The refined parameters for each shell include i) the mean interatomic distance between the absorber and the scattered atoms (R in Å; not systematically fitted as free parameter), and ii) the mean-square relative Debye-Waller factor per scatterer ($\sigma^2$ in $Å^{-2}$). For each fit, the number of fitted parameters (maximum 11) are kept below the number of independent points to ensure that the degree of freedom (of 17) is maximised and the fit is relevant.

## Supplementary Table

**Table S-1** Interatomic distances of the 2nd and the 3rd nearest neighbours in FAp (Hughes *et al.*, 1990) for **(a)** Ca(1) site and **(b)** Ca(2) site. CN, coordination number.

| a) Ca(1) site | CN | Distance (Å) |
|---|---|---|
| P | 3 | 3.21 |
| $Ca_1$ | 1 | 3.43 |
| $Ca_1$ | 1 | 3.45 |
| P | 3 | 3.58 |
| O | 3 | 3.92 |
| $Ca_2$ | 3 | 3.96 |
| $Ca_2$ | 3 | 4.05 |
| **b) Ca(2) site** | **CN** | **Distance (Å)** |
| P | 1 | 3.08 |
| P | 1 | 3.26 |
| O | 2 | 3.35 |
| O | 1 | 3.49 |
| P | 1 | 3.49 |
| P | 2 | 3.70 |
| $Ca_1$ | 2 | 3.96 |
| O | 3 | 3.99 |
| $Ca_2$ | 2 | 4.00 |
| $Ca_1$ | 2 | 4.05 |
| $Ca_2$ | 4 | 4.14 |

## Supplementary Figures

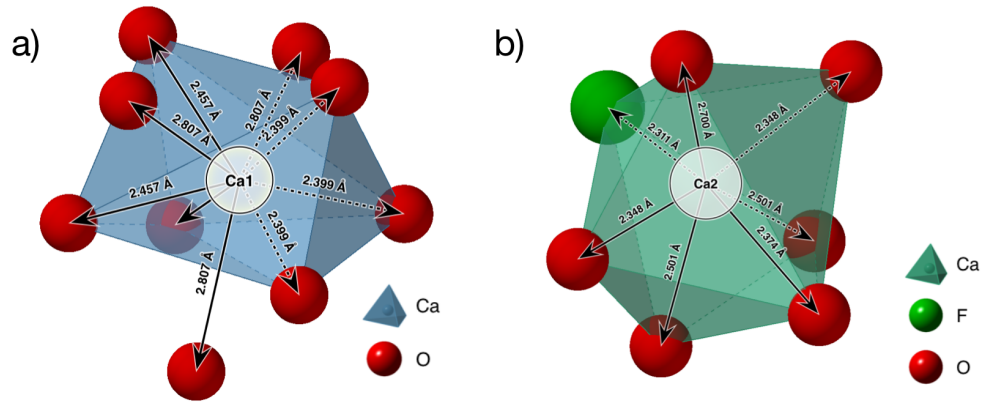


| Bond | Distance (Å) |
|---|---|
| $Ca_1$-O | 2.40 |
| $Ca_1$-O | 2.40 |
| $Ca_1$-O | 2.40 |
| $Ca_1$-O | 2.46 |
| $Ca_1$-O | 2.46 |
| $Ca_1$-O | 2.46 |
| $Ca_1$-O | 2.81 |
| $Ca_1$-O | 2.81 |
| $Ca_1$-O | 2.81 |
| Mean Distance: 2.55 Å | |

| Bond | Distance (Å) |
|---|---|
| $Ca_2$-F | 2.31 |
| $Ca_2$-O | 2.35 |
| $Ca_2$-O | 2.35 |
| $Ca_2$-O | 2.37 |
| $Ca_2$-O | 2.50 |
| $Ca_2$-O | 2.50 |
| $Ca_2$-O | 2.70 |
| Mean Distance: 2.44 Å | |

**Figure S-1** Geometric model of the Ca 1st nearest neighbours polyhedra in FAp with corresponding tables of interatomic distances (Hughes *et al.*, 1990). **(a)** Ca(1) site corresponding to 6+3-fold coordination as a distorted tricapped trigonal prism. **(b)** Ca(2) site corresponding to 7-fold coordination as a distorted pentagonal bipyramid.

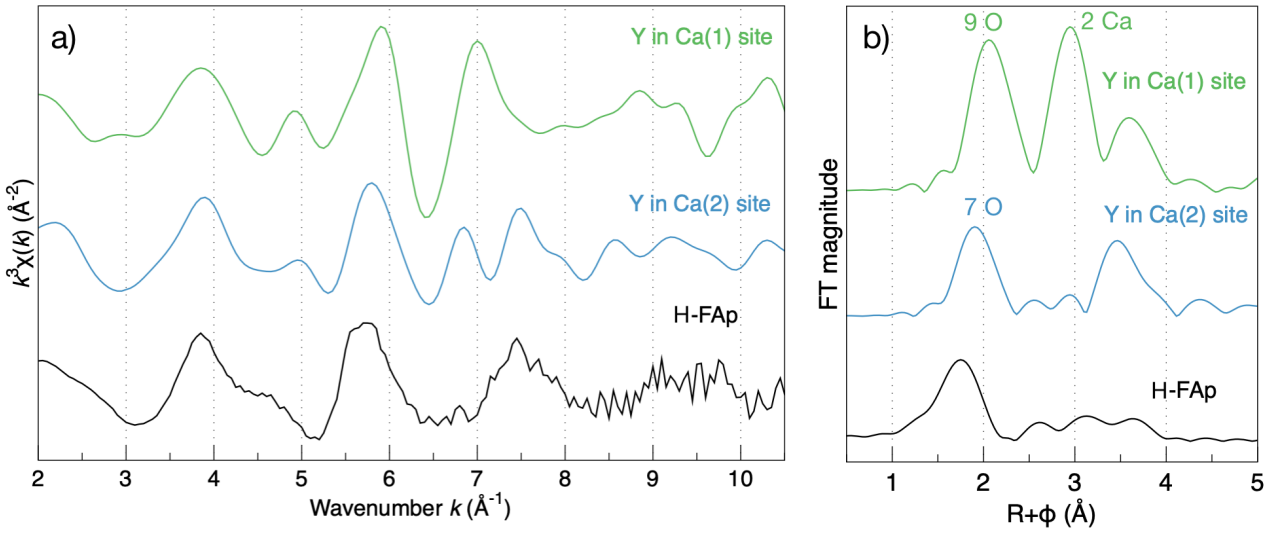


**Figure S-2** **(a)** Qualitative comparison of the Y *K*-edge $k^3$-weighted EXAFS spectra obtained for H-FAp, with theoretical EXAFS calculations (*FEFF10*) of Y in Ca(1) site (green line) and in Ca(2) site (blue line). **(b)** Corresponding Fourier Transform. The Ca(1) site clearly differs from the others with a significant shift to higher distances of the O 1st neighbours contribution, and a strong contribution of the Ca 2nd neighbours.

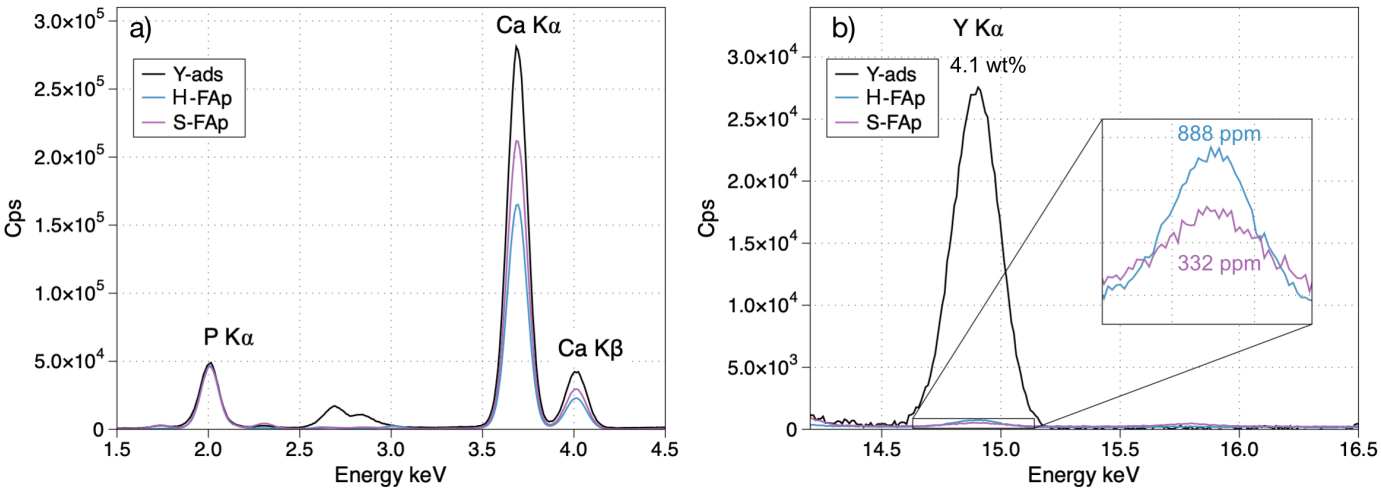


**Figure S-3** X-ray fluorescence spectra of Y-ads (black line), magmatic fluorapatite (H-FAp, blue line), sedimentary fluorapatite (purple line) with corresponding Y concentrations, centred around P and Ca emission lines **(a)** and around the Y emission line **(b)**.

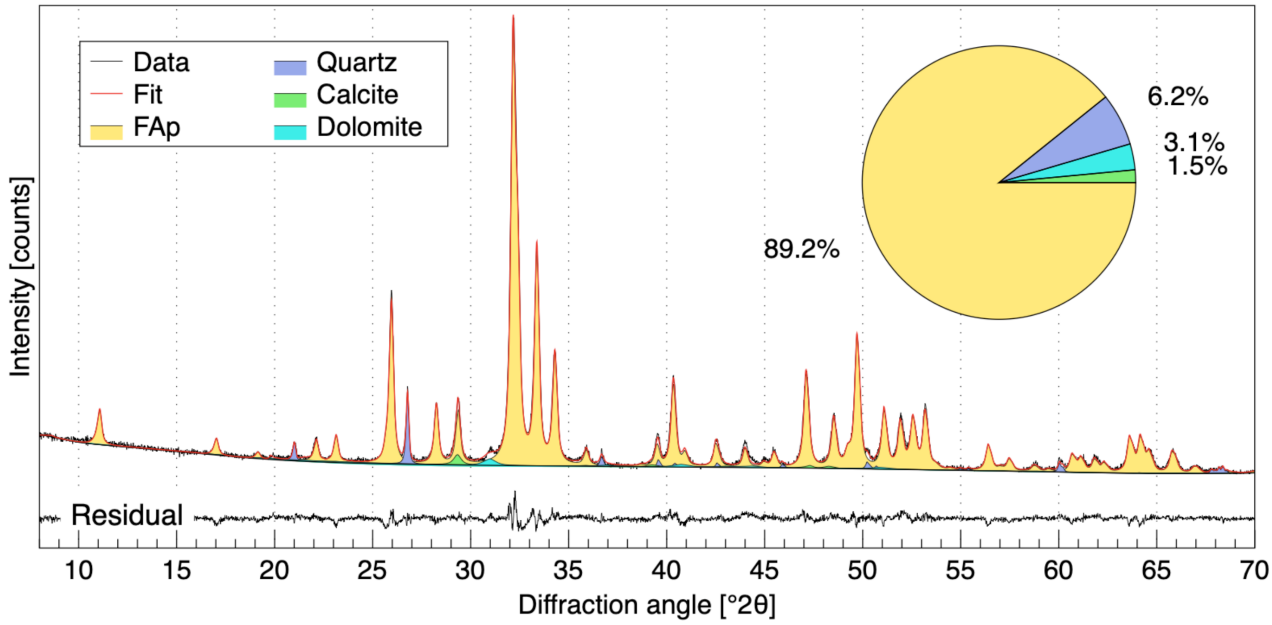


**Figure S-4** Mineralogical proportions in wt. % of the Moroccan phosphorite sample estimated by Rietveld refinement. Results are not normalised to 100 % and the overall $\chi^2$ equals to 2.66.

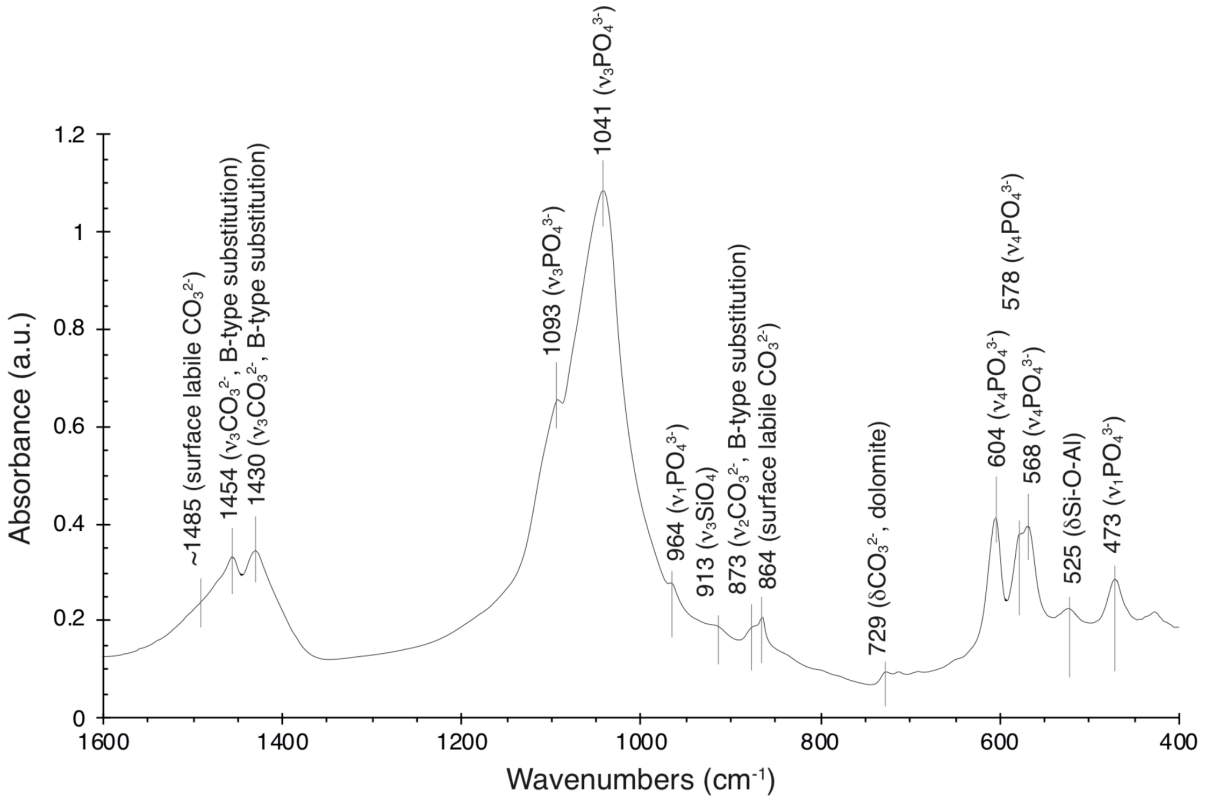


**Figure S-5** FTIR spectra of sedimentary sample. The interval from 1600 to 400 $cm^{-1}$ highlights the four $PO_4$ internal vibrational modes as well as structural $CO_3^{2-}$ vibration modes typical of the B-type carbonated FAp.

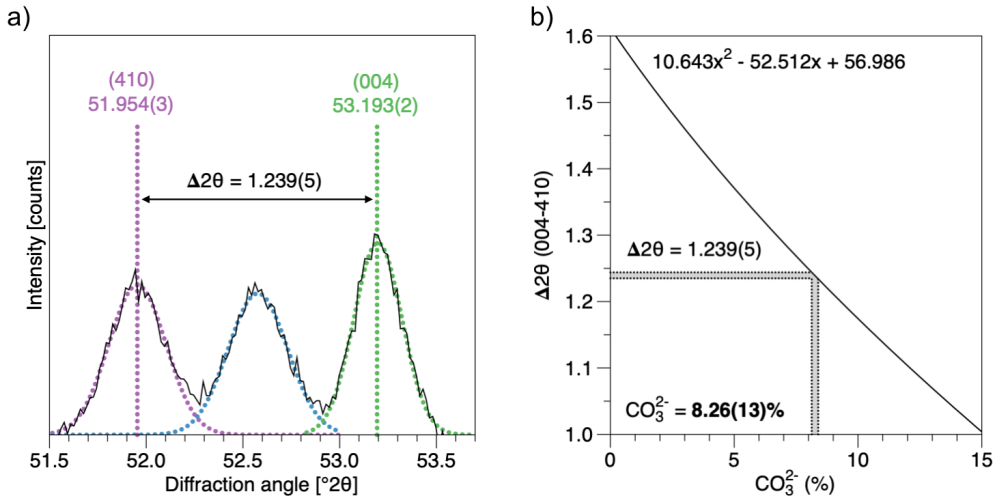


**Figure S-6** **(a)** Positions of the (410) and (004) XRD reflections on the sedimentary sample using a gaussian fit to estimate the value of Δ2θ (004)-(410); **(b)** estimated $CO_3^{2-}$ content (%) for the S-FAp, carbonate concentration (%) in B-type FAp calculated using the empirical equation of Schuffert *et al*. (1990), where *x* stands for Δ2θ (004)-(410).

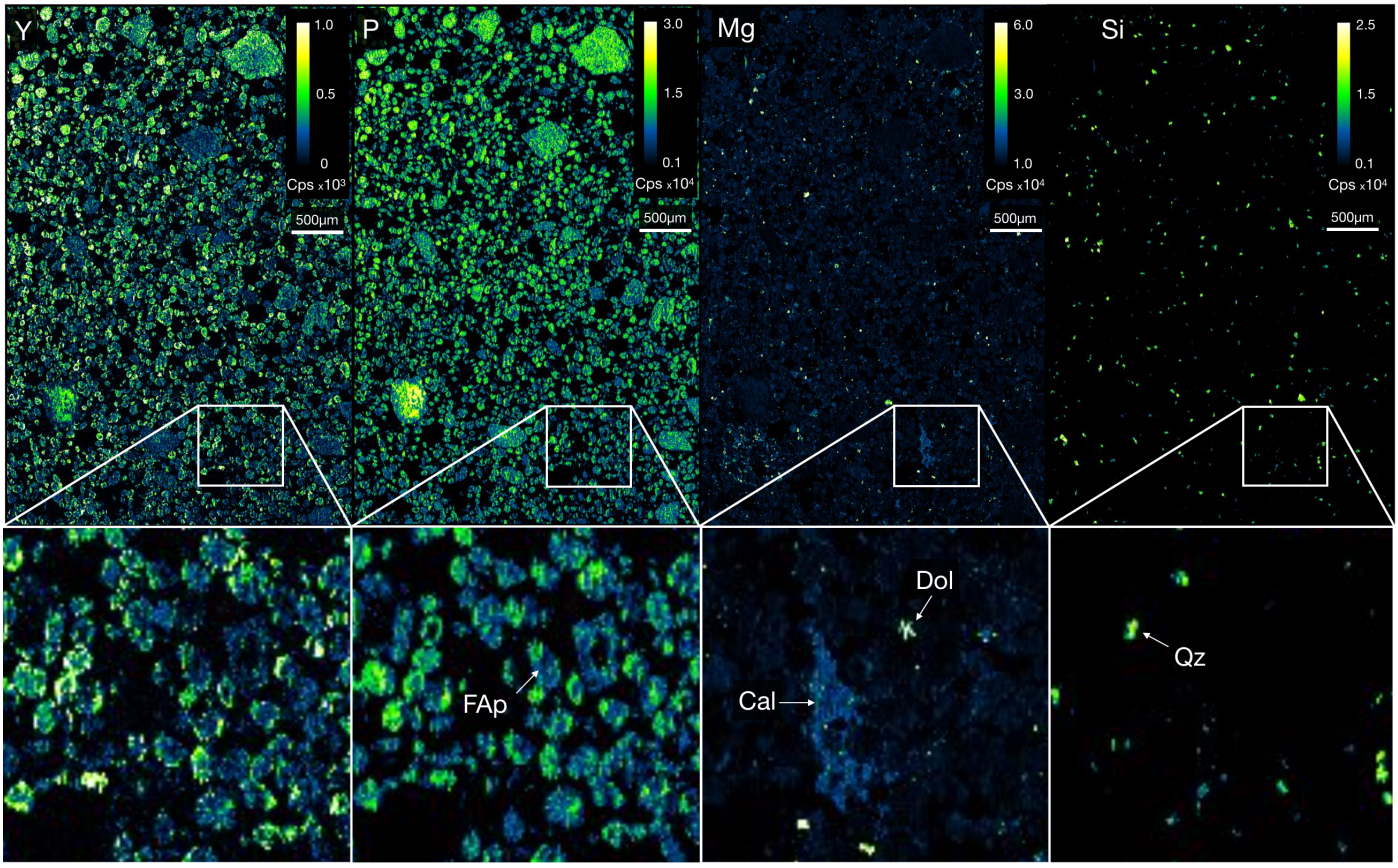


**Figure S-7** Laser Induced Breakdown Spectroscopy (LIBS) elemental distribution map of Y compared to those of P, Mg, and Si, showing the presence of fluorapatite, carbonates and quartz, respectively. Top, large-scale maps covering a 9 × 16 mm area. Bottom, maps of smaller areas that contain all mineral phases identified by X-ray diffraction. Note that Y is exclusively distributed in fluorapatite grains (S-FAp).

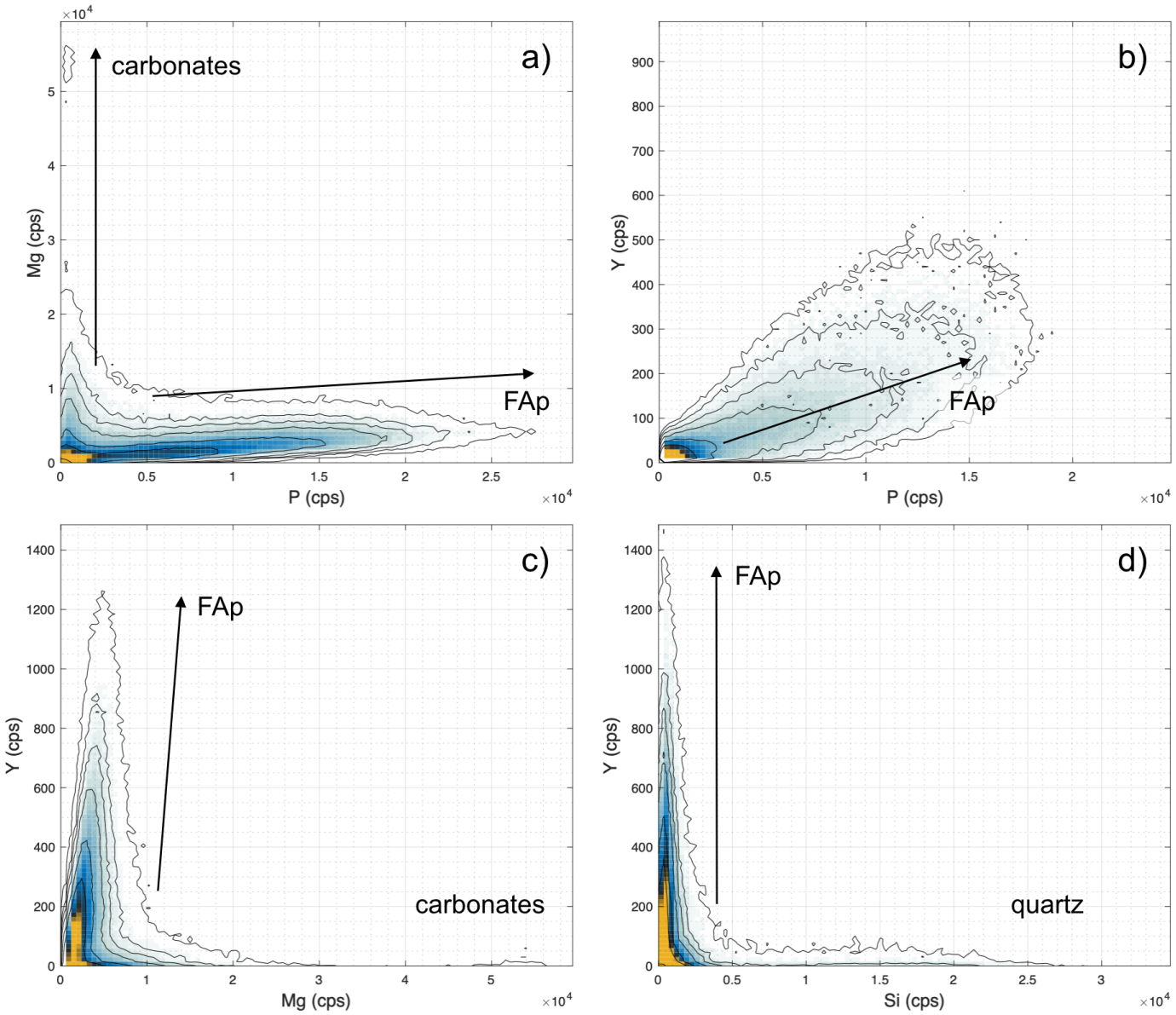


**Figure S-8** Correlation density plots (in number of counts) of large-scale LIBS elemental maps (Fig. S-7). **(a)** Mg *vs*. P, **(b)** Y *vs*. P, **(c)** Y *vs*. Mg, **(d)** Y *vs*. Si. Note that Y is correlated to FAp (b and c), while anti-correlated to carbonates and quartz (c and d, respectively).

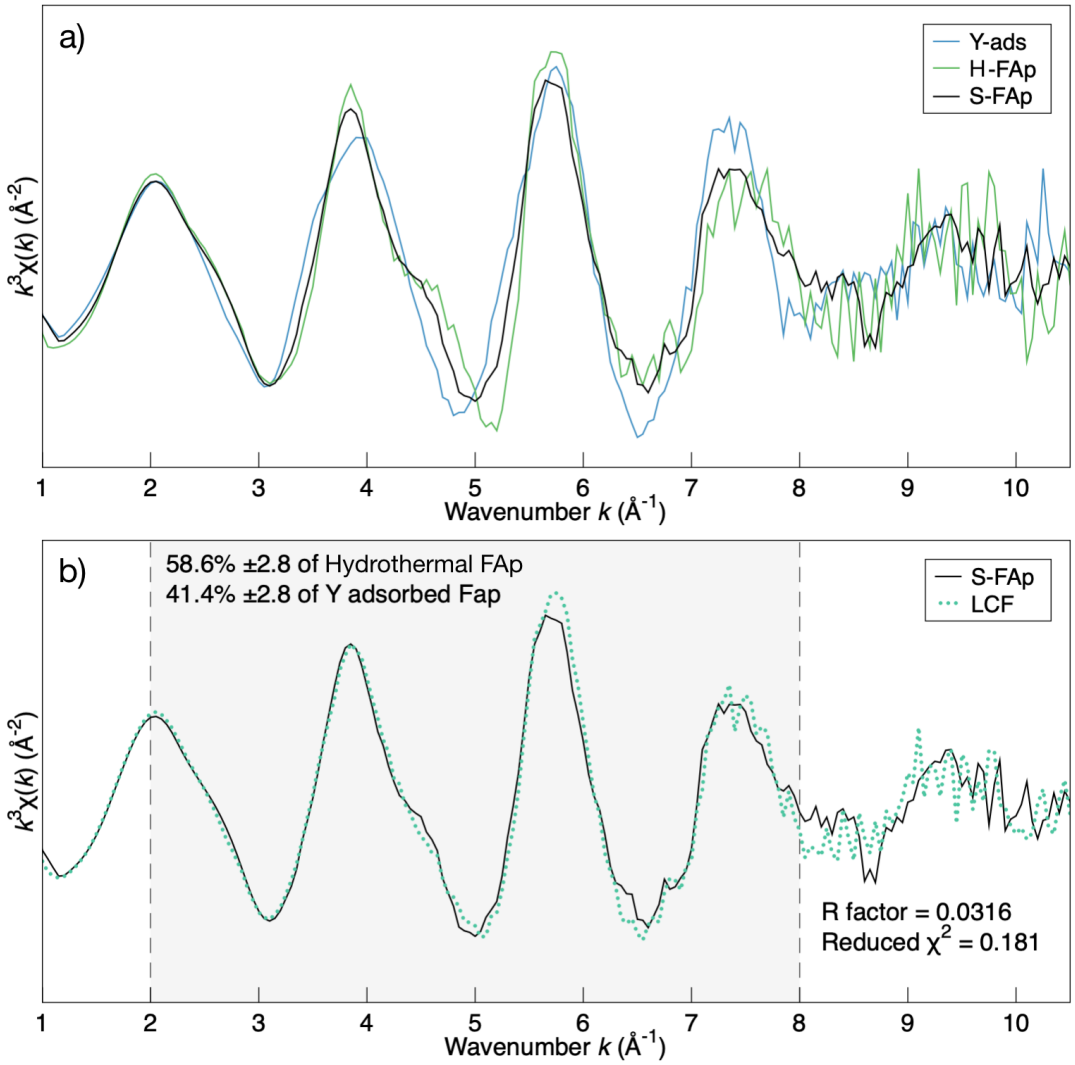


**Figure S-9** **(a)** EXAFS comparison of the S-FAp (black line), H-FAp (green line), and Y-ads (blue line). **(b)** Results of the sedimentary FAp EXAFS LCF (blue-green line) using Y-ads and H-FAp as pure components.

## Supplementary Information References

Borst, A.M., Smith, M.P., Finch, A.A., Estrade, G., Villanova-de-Benavent, C., Nason, P., Marquis, E., Horsburgh, N.J., Goodenough, K.M., Xu, C., Kynický, J., Geraki, K. (2020) Adsorption of rare earth elements in regolith-hosted clay deposits. *Nature Communications* 11, 4386. https://doi.org/10.1038/s41467-020-17801-5

Cáceres, J.O., Pelascini, F., Motto-Ros, V., Moncayo, S., Trichard, F., Panczer, G., Marin-Roldan, A., Cruz, J.A., Coronado, I., Martin-Chivelet, J. (2017) Megapixel multi-elemental imaging by Laser-Induced Breakdown Spectroscopy, a technology with considerable potential for paleoclimate studies. *Scientific Reports* 7, 5080. https://doi.org/10.1038/s41598-017-05437-3

Chew, D.M., Petrus, J.A., Kamber, B.S. (2014) U–Pb LA–ICPMS dating using accessory mineral standards with variable common Pb. *Chemical Geology* 363, 185–199. https://doi.org/10.1016/j.chemgeo.2013.11.006

Döbelin, N., Kleeberg, R. (2015) *Profex*: a graphical user interface for the Rietveld refinement program *BGMN*. *Journal of Applied Crystallography* 48, 1573–1580. https://doi.org/10.1107/s1600576715014685

El Bamiki, R., Raji, O., Ouabid, M., Elghali, A., Yazami, O.K., Bodinier, J.-L. (2021) Phosphate Rocks: A Review of Sedimentary and Igneous Occurrences in Morocco. *Minerals* 11, 1137. https://doi.org/10.3390/min11101137

Faucher, M., Pannetier, J. (1980) Refinement of the $Y_2O_3$ structure at 77 K. *Acta Crystallographica Section B* 36, 3209–3211. https://doi.org/10.1107/S0567740880011351

Gleason, J.D., Marikos, M.A., Barton, M.D., Johnson, D.A. (2000) Neodymium isotopic study of rare earth element sources and mobility in hydrothermal Fe oxide (Fe-P-REE) systems. *Geochimica et Cosmochimica Acta* 64, 1059–1068. https://doi.org/10.1016/S0016-7037(99)00325-7

Graf, D.L. (1961) Crystallographic tables for the rhombohedral carbonates. *American Mineralogist* 46, 1283–1316. http://www.minsocam.org/ammin/AM46/AM46_1283.pdf

Hughes, J.M., Cameron, M., Crowley, K.D. (1990) Crystal structures of natural ternary apatites: Solid solution in the $Ca_5(PO_4)_3X$ (X=F, OH, Cl) system. *American Mineralogist* 75, 295–304. http://www.minsocam.org/ammin/AM75/AM75_295.pdf

Kashiwabara, T., Toda, R., Nakamura, K., Yasukawa, K., Fujinaga, K., Kubo, S., Nozaki, T., Takahashi, Y., Suzuki, K., Kato, Y. (2018) Synchrotron X-ray spectroscopic perspective on the formation mechanism of REY-rich muds in the Pacific Ocean. *Geochimica et Cosmochimica Acta* 240, 274–292. https://doi.org/10.1016/j.gca.2018.08.013

Levien, L., Prewitt, C.T., Weidner, D.J. (1980) Structure and elastic properties of quartz at pressure. *American Mineralogist* 65, 920–930. http://www.minsocam.org/ammin/AM65/AM65_920.pdf

Lyons, J.I. (1988) Volcanogenic iron oxide deposits, Cerro de Mercado and vicinity, Durango. *Economic Geology* 83, 1886–1906. https://doi.org/10.2113/gsecongeo.83.8.1886

Mathon, O., Beteva, A., Borrel, J., Bugnazet, D., Gatla, S., Hino, R., Kantor, I., Mairs, T., Munoz, M., Pasternak, S., Perrin, F., Pascarelli, S. (2015) The time-resolved and extreme conditions XAS (TEXAS) facility at the European Synchrotron Radiation Facility: the general-purpose EXAFS bending-magnet beamline BM23. *Journal of Synchrotron Radiation* 22, 1548–1554. https://doi.org/10.1107/s1600577515017786

Motto-Ros, V., Gardette, V., Sancey, L., Leprince, M., Genty, D., Roux, S., Busser, B., Pelascini, F. (2020) LIBS-Based Imaging: Recent Advances and Future Directions. *Spectroscopy* 35, 34–40. https://hal.science/hal-02998713

Muñoz, M., Argoul, P., Farges, F. (2003) Continuous Cauchy wavelet transform analyses of EXAFS spectra: A qualitative approach. *American Mineralogist* 88, 694–700. https://doi.org/10.2138/am-2003-0423

Newville, M. (2001) *IFEFFIT*: Interactive XAFS analysis and *FEFF* fitting. *Journal of Synchrotron Radiation* 8, 322–324. https://doi.org/10.1107/S0909049500016964

Ravel, B., Newville, M. (2005) *ATHENA, ARTEMIS, HEPHAESTUS*: data analysis for X-ray absorption spectroscopy using *IFEFFIT*. *Journal of Synchrotron Radiation* 12, 537–541. https://doi.org/10.1107/s0909049505012719

Regnier, P., Lasaga, A.C., Berner, R.A., Han, O.H., Zilm, K.W. (1994) Mechanism of $CO_3^{2-}$ substitution in carbonate-fluorapatite: Evidence from FTIR spectroscopy, $^{13}C$ NMR, and quantum mechanical calculations. *American Mineralogist* 79, 809–818. http://www.minsocam.org/ammin/AM79/AM79_809.pdf

Schuffert, J.D., Kastner, M., Emanuele, G., Jahnke, R.A. (1990) Carbonate-ion substitution in francolite: A new equation. *Geochimica et Cosmochimica Acta* 54, 2323–2328. https://doi.org/10.1016/0016-7037(90)90058-S